LUND UNIVERSITY

Ultrawideband MIMO Channel Measurements and Modeling in a Warehouse Environment

Sangodoyin, Seun; He, Ruisi; Molisch, Andreas F.; Kristem, Vinod; Tufvesson, Fredrik

Link to publication

Ultrawideband MIMO Channel Measurements and Modeling in a Warehouse Environment

Seun Sangodoyin, *Student Member, IEEE*, Ruisi He, *Member, IEEE*, Andreas F. Molisch, *Fellow, IEEE*, Vinod Kristem *Student Member, IEEE* and Fredrik Tufvesson, *Senior Member, IEEE*

Abstract—This paper presents a detailed description of a propagation channel measurement campaign performed in a warehouse environment and provide a comprehensive channel model for this environment. Using a vector network analyzer, we explored both line-of-sight and non-line-of-sight scenarios over a 2-8 GHz frequency range. We extracted both small-scale and large-scale channel parameters such as distance-dependent pathloss exponent , frequency-dependent pathloss exponent, shadowing variance, and amplitude fading statistics of the channel. We also provide the clustering analysis of the channel impulse responses by using a modified *Saleh-Valenzuela* approach. Our model is validated by comparing the distributions of the root-mean-square delay spread obtained from our model and measurement data, respectively. The model developed can be used for realistic performance evaluations of ultrawideband (UWB) communications and localization systems in warehouse environments.

Index Terms—Propagation channel, ultrawidebandwidth, UWB, MIMO, statistical channel model, warehouse environment

I. INTRODUCTION

Ultrawideband (UWB) wireless systems have been embraced as a means for both high and low data-rate communications, as well as localization systems [1]. UWB systems are typically defined to have more than 500 MHz of bandwidth or more than 20% relative bandwidth and authorized to operate without license in the 3.1-10.6 GHz frequency band by the Federal Communications Commission (FCC) [2] in the US. UWB signaling has a number of attractive qualities, including low sensitivity to fading, easier material penetration and fine delay resolution. Wireless systems that operate over UWB channels promise enhanced multiple access [3] and significant improvement in resolution of tracking, localization and ranging purposes [4]. Consequently, UWB technology has found use in a variety of applications including wireless sensor networks [5] and - as of late - Radio-frequency identification (RFID) technology. It is noteworthy that UWB-based localization systems (including RFID) are naturally deployed in warehouse environments, and also UWB-based sensor networks and communications systems will be used in such environments.

Accurate channel models are required for the development of any wireless communication systems, hence it is of utmost importance that the channel in which the wireless system is to be deployed be duly characterized through propagation channel measurements. Although there have been a number of UWB channel measurements and resulting models in environments such as indoor-residential [6], office, and industrial [7], to the best of the authors' knowledge, there are no such investigations for warehouse environments. The distinctive properties of warehouse propagation channels are not only in the content stored (i.e., boxes, computers, furniture etc,) but also the geometric layout (often sparse with storage racks or shelves all demarcated into aisles). There is thus a need to characterize this channel if UWB systems are to be deplored in it.

In this paper, we present a detailed description of a UWB propagation channel measurement campaign performed in a warehouse environment. We explored various scenarios such as line-of-sight (LOS) and non-LOS (NLOS). We present results for key channel parameters such as distance-dependent pathloss exponent, (n), frequency-dependent pathloss coefficient (κ), shadowing gain (X_σ), amplitude fading statistics and a clustering model for multipath components (MPCs) in the environment.

The rest of the paper is organized as follows. Section II describes the measurement environment. Section III describes our measurement setup and parameter configuration. Data processing procedure and results obtained are described in Section IV. Section V provides a model validation. Conclusions are drawn in Section VII.

II. MEASUREMENT ENVIRONMENT

The measurement campaign was performed in a warehouse facility at the University of Southern California (USC) in Los Angeles, California. The warehouse is a four-storey building comprising of large open halls (shown in Fig. 1) on each floor for storing items such as books, computers, and stationary. The ceiling, floor and walls surrounding each large open hall are all made of reinforced bricks and concrete, while steel-concrete pillars served as structural supports for the ceiling in the warehouse (these can act as scatterers as well as contribute to shadowing effects in the propagation channel). The storage halls were demarcated into several aisles, with each aisle comprising of rows of two layered metallic storage racks. Walkways/paths are available between aisles to ease the movement of people and forklift trucks moving boxes in and out of the warehouse. Also, demarcations are made with barbed-wired fences to store sensitive materials such as medical equipment, non-toxic laboratory chemicals etc. Access to each storage hall is mainly through steel garage doors, (which could serve as a source of reflections in the channel). The measurements were conducted on the first floor storage halls and basement storage halls of the warehouse

Fig. 1. USC Warehouse Facility

Fig. 2. Floor map of the first floor of the warehouse

respectively. The floor plan of the measurement venue is shown[1] in Fig. 2. In our measurements, we selected 5 positions for the LOS scenario at each TX-RX distance separation, while 8 positions were selected for the NLOS scenarios. These positions experience different surrounding objects and are thus suitable for analyzing the shadowing statistics of the channel. The TX-RX distance separations measured were 5, 10, 15, 20, and 25 m respectively in both cases (i.e., LOS and NLOS). The measured positions are indicated in Fig. 2. The TX/RX locations for the LOS/NLOS measurements are indicated on the floor map with the abbreviations TXL1-(indicating TX LOS position 1) and TXN1- (indicating TX NLOS position 1), etc., while the same format is used for the receiver positions.

III. MEASUREMENT SETUP

The measurement campaign was performed using a frequency domain channel sounder setup with a stepper motor for antenna positioning (see Fig. 3). At the heart of the channel sounder setup is a vector network analyzer (VNA, HP 8720ET), which is used for obtaining the complex transfer function ($H(f)$) of the propagation channel. The VNA was calibrated at the antenna feed points and a stepped frequency sweep was conducted for 1601 points in the 2-8 GHz frequency range. The parameter settings for the channel measurement are shown in Table II below. In order to be able to extract small-scale fading statistics, transmit and receive antennas were each moved over 8 positions. Specifically, a single ultrawideband (custom-built) omni-directional antenna was attached to a 1.78 m pole and then fastened to a stepper-motor controlled linear positioner at both transmitter and receiver ends. The antenna was moved to different positions along the rails of the positioner. The separation between antenna position is 50 mm, hence by moving each antenna over a distance of 400 mm at both ends, 8 positions at each link end are measured, providing a total of 64 channel realizations. With the array positioner movement time and VNA frequency

[1]The floormap for the basement is not shown here due to space constraints, however all floor plans have similar layout
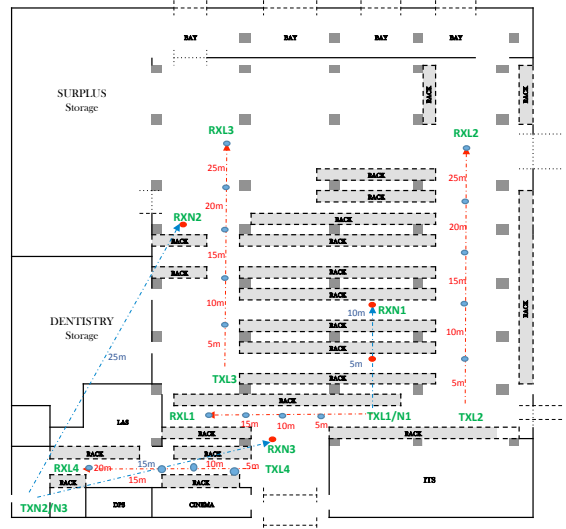
TABLE I
HARDWARE USED IN THE UWB MIMO CHANNEL MEASUREMENT

Item	Manufacturer	Model No.
VNA	Agilent	8720ET
positioner	Velmex	MN80-0200-E01-21
Antennas	XY	XY2
LNA	SCA	SCA04/239
Motor control	Velmex	VMX-2

TABLE II
CHANNEL MEASUREMENT PARAMETERS

Parameter	Setting
Bandwidth	6GHz (2GHz-8GHz)
Center frequency, f_c	6GHz
Total number of Channels	64
Number of sub-carriers	1601
delay resolution	0.167ns
Frequency resolution	3.74MHz
Maximum path length	80m

sweep time (over 6 GHz bandwidth) taken into consideration, the total measurement time for each position (64 sub-channels) was about 48 minutes. Note that our setup can also be interpreted as a *virtual* uniform linear array (ULA), which allows to extract directional characteristics of the channel. Such directional results will be presented in [8].

A key assumption for our measurement is to that channel is *stationary*, which is fulfilled if the scatterers and other environmental objects are not moving. We thus made sure that there were no moving object, forklift trucks or personnel, etc. during the measurement campaign. We also ensured that the cables used do not twist and turn during the positioner movement.

IV. DATA PROCESSING AND RESULTS

After each measurement run, the data captured from the VNA is processed offline in order to extract the channel transfer function. We denoted the transfer function as
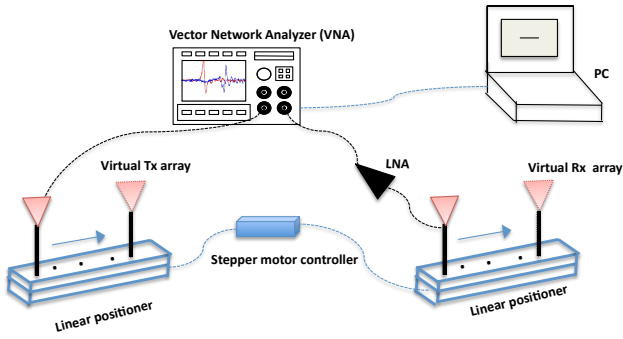
Fig. 3. Channel sounder measurement setup in the warehouse environment

	n	G_{d_0}(dB)	κ	σ(dB)
LOS	1.63	-38.26	1.33	2.86
NLOS	2.14	-49.06	1.33	2.84

$H(d, S_d, m_{\mathrm{R}}, m_{\mathrm{T}}, f_k)$, where $m_{\mathrm{T}} = 1...M_{\mathrm{T}}$ and $m_{\mathrm{R}} = 1...M_{\mathrm{R}}$ denote the TX and RX antenna positions, $f_k = 1...M_f$ represents the frequency points , $d = 1...D$ is the distance measured, and shadowing locations are represented by $S_d = 1...M_{S_d}$. In our measurements, $M_{\mathrm{R}}, M_{\mathrm{T}} = 8$ respectively, while the number of frequency points $M_f = 1601$. As mentioned above, a total of $D = 5$ different distances were measured of which were $d = \{5, 10, 15, 20, 25\}$ m. The number of shadowing points (at each measured distance d) M_{S_d} is 5 and 8 for LOS and NLOS cases, respectively. The measured $H(d, S_d, m_{\mathrm{R}}, m_{\mathrm{T}}, f_k)$ was transformed to the delay domain by using an inverse Fourier transform; the resulting impulse response is denoted as $h(d, S_d, m_{\mathrm{R}}, m_{\mathrm{T}}, \tau_k)$; a Hann instantaneous window was applied to suppress temporal side lobes. From the impulse response, the power-delay-profile (PDP), i.e., $P(d, S_d, m_{\mathrm{R}}, m_{\mathrm{T}}, \tau_k) = |h(d, S_d, m_{\mathrm{R}}, m_{\mathrm{T}}, \tau_k)|^2$ can be obtained. For each shadowing location, the influence of small-scale fading is removed by averaging the instantaneous PDPs over the 8x8 TX/RX positions to obtain the average-power-delay-profile (APDP, $\hat{P}(d, S_d, \tau_k)$).

$$\hat{P}(d, S_d, \tau_k) = \frac{1}{M_{\mathrm{T}} \cdot M_{\mathrm{R}}} \sum_{m_{\mathrm{T}}}^{M_{\mathrm{T}}} \sum_{m_{\mathrm{R}}}^{M_{\mathrm{R}}} P(d, S_d, m_{\mathrm{R}}, m_{\mathrm{T}}, \tau_k) \quad (1)$$

To reduce the influence of noise, we implement a noise-threshold filter, which sets all APDP samples whose magnitude is below a certain threshold to zero. The threshold value is chosen to be 6 dB above the noise floor of the APDP. This noise floor is computed by averaging the energies in all bins with delays shorter than that of the first MPC of the APDP. Also, the APDP was subjected to a delay-gating filter, which eliminates all MPCs whose delays are 60 m or more in excess of the TX-RX separation.

A. Pathloss Analysis

From the APDP and channel transfer function at different measured locations, we are able to extract parameters such as the distance-dependent pathloss exponent (n), frequency-dependent pathloss component (κ), amplitude fading statistics, shadowing, etc. These parameters are shown in Table III below, while example APDP plots for both LOS and NLOS measurements at 5 and 25 m distances are shown in Figs. 5 and 6.

It has been suggested in the literature [9], to simplify pathloss modeling by decomposing the pathloss of a propagation channel into independent functions of distance and frequency, $G_{d,f} = G_d \cdot G_f$, where the distance dependent pathloss function (G_d) can be modeled using a conventional power-law,

$$G_d(\mathrm{dB}) = G_{d_0} - 10 \cdot n \cdot \log_{10}\left(\frac{d}{d_0}\right) + X_\sigma(\mathrm{dB}) \quad (2)$$

where n is the pathloss exponent, d_0 is the reference distance, G_{d_0} is the pathloss at the reference distance and X_σ is the shadowing gain, The dB value of the shadowing gain is assumed to have a Gaussian distribution with standard deviation σ. The distance-dependent pathloss component for the LOS and NLOS scenario obtained from our analysis can be visualized from the scatter plot shown in Fig. 4.
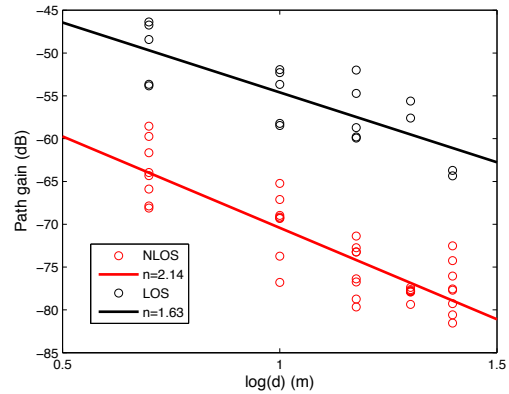

Fig. 4. Distance dependency of the path gain.

The frequency-dependence of the pathloss (G_f) primarily arises from the antenna power area density and gain variations with frequency and additionally from frequency dependence of physical propagation phenomena such as scattering and diffraction. In our model, G_f is expressed as a power-law decay model [10] which in logarithmic form becomes

$$G_f(\mathrm{dB}) = G_{f0} - 20 \cdot \kappa \cdot log_{10}\left(\frac{f}{f_{Mc}}\right) \quad (3)$$

where κ is the frequency decay factor. G_{f0} is the power of the lowest frequency sub-band, f_{Mc} is the center frequency of each selected sub-band is 500MHz (each sub-band has a bandwidth of 500MHz with f_{Mc} = 2.5GHz, 3GHz, ... , 7.5GHz).

B. The Small-Scale Statistics

The variation in the received signal amplitude over the positions within a fading location can be attributed to the
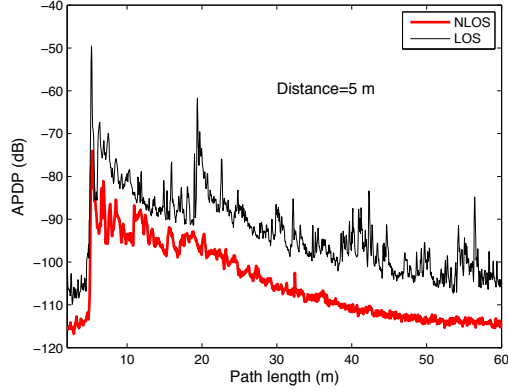
Fig. 5. Example plots of one APDP for 5 m.

Fig. 6. Example plots of one APDP for 25 m.

small-scale fading in the environment. To find a statistical distribution of the amplitude fading in our measurement environment, empirical data from delay bins at specific excess delays [2] were matched to some typical theoretical distributions such as Rayleigh, lognormal, Nakagami, and Weibull. We have used both the Kolmogorov-Smirnov (K-S) and Chi-square (χ^2) hypothesis tests to determine the goodness-of-fit for these distributions at 5% significant level. Table IV below compares the passing rate of these tests for our measurement data for both the LOS and NLOS scenario. It is clear that the Nakagami distribution has a much higher passing rate. This is in line with various previous measurements of UWB fading statistics.

For the Nakagami distribution, the m-parameter was computed using the inverse normalized variance (INV) estimator.

$$\hat{m}_{INV} = \frac{\mu_2^2}{\mu_4 - \mu_2^2} \quad (4)$$

where $\mu_{\hat{k}} = \frac{1}{N} \sum_{i=1}^{N} A_i^{\hat{k}}$, A is the observed amplitude vector of the measurement data and $N = 64$ in this case, $\hat{k}$-moment order. The m-parameters for each bin are random variables and were modeled by a truncated Gaussian distribution in [11] denoted by $m \sim T_N(\mu_m, \sigma_m^2)$. Using a similar assumption in our measurement, we obtain the following model for the m-parameter using the probability density function:

$$f_m(x) = \sim \begin{cases} \rho_m e^{-((x-\mu_m)^2/2\sigma_m^2)}, & \text{if } x \geq 0.5 \\ 0, & \text{otherwise} \end{cases} \quad (5)$$

where ρ_m is the normalization constant chosen so that the integral over $f_m(x)$ is unity. To parameterize the proposed truncated Gaussian distribution, the mean (μ_m) and variance (σ_m) values of the m-parameter as a function of excess delay were obtained by using a linear regression fit

$$\mu_m(\tau_k) = A - \frac{1}{B}\tau_k \quad (6)$$

TABLE IV
PASSING RATE OF K-S AND χ^2 HYPOTHESIS TEST AT 5% SIGNIFICANCE LEVEL

Distributions	LOS		NLOS	
	K-S	χ^2	K-S	χ^2
Weibull	85.25	71.25	89.01	70.10
Lognormal	82.50	52.09	36.27	7.52
Rayleigh	83.53	65.93	27.22	32.40
Nakagami	95.07	88.11	97.45	80.39

TABLE V
REGRESSION LINE PARAMETERS FOR m-PARAMETER CHARACTERIZATION

	A	B	C	D
LOS	1.2	1361	0.61	227
NLOS	1.45	1914	0.25	5128

$$\sigma_m(\tau_k) = C - \frac{1}{D}\tau_k \quad (7)$$

where the units of τ_k[3] are in nanoseconds. The slope and intercept values for different scenarios in our experiments are stated below in Table V.

C. Clustering Analysis

The MPCs are arriving in clusters, as can be seen from Figs. 5 and 6. Determining the clusters from the delay measurements only is difficult, and automated algorithms are sensitive to model mismatch - a fact well established in the literature. We thus follow the approach of visual clustering in our analysis. The extracted clusters are then modeled following the widely-used Saleh-Valenzuela (SV) model [12], though we introduce some modifications as elaborated below.

We observed in our analysis that the first arriving MPC happens to be the strongest in the LOS and NLOS scenarios when the distance between TX and RX is small (e.g., 5 m, 10 m), as shown in Fig. 5, however, this situation changes drastically for NLOS cases with larger TX-RX separations (20 m, 25 m), as depicted in Fig. 6. There, we observed that the strongest MPC of the APDP occurs much later than the

[2]To ensure proper characterization of the fading statistics per delay bin in our analysis, a runtime compensation for every MPC in the impulse response was performed by translating the bin with the *quasi*-LOS component to the first bin of the impulse response
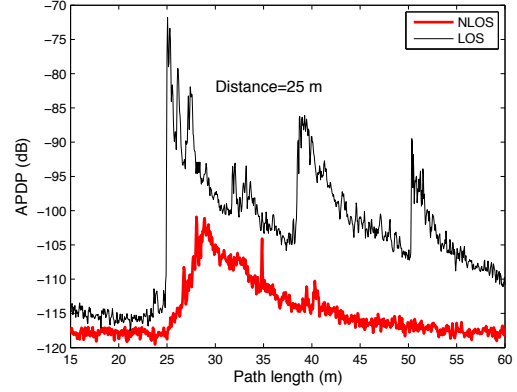
[3]Note that the k subscript indicates the delay bin index

arrival of the first MPC. For the LOS and NLOS scenarios with small TX-RX separation, the cluster powers exhibit a classical exponential decay. For the NLOS measurements over large distances however, we observed that the clusters after the strongest MPC does exhibit an exponential decay while there were in-fact distinct contributions before the strongest MPCs which constitute a "soft onset" with a negative cluster power decay constant. This is in line with previous observations in e.g. industrial environments [7]. Since two types of APDP shapes are observed in the measurements, we divide the analysis of the APDPs into two groups:

- Group 1, which contains all the LOS measurements and the NLOS measurements for shorter TX - RX separation. The APDPs of Group 1 have a strong first MPC and the strength of the following clusters decreases exponentially with delay. The APDPs of Group 1 can be perfectly modeled by the standard SV model.
- Group 2, which contains the NLOS measurements for larger TX-RX separation. The strongest MPC in APDPs of Group 2 comes tens of nanoseconds after the first component. After the strongest MPC, the APDPs consist of one or several clusters with an exponential decay; while before the strongest MPCs , the APDPs have a soft onset of several "reverse clusters", whose strength increases exponentially with delay. The slope of the APDPs before the strongest MPCs is found to be larger than the slope after.

In the SV model, the impulse response is described as

$$h(t) = \sum_{c=0}^{\infty} \sum_{r=0}^{\infty} \alpha_{rc} \exp(j\theta_{rc}) \delta(t - T_c - \tau_{rc}) \qquad (8)$$

where α_{rc} and θ_{rc} are the gain and phase of the rth ray of the cth cluster, respectively. T_c is the arrival time of the cth cluster. τ_{rc} is the arrival time of the rth ray within the cth cluster. The peak gain is determined by

$$|\alpha_{rc}(T_c, \tau_{rc})|^2 = |\alpha_{rc}(0,0)|^2 \exp(-\frac{T_c}{\gamma_c}) \exp(-\frac{\tau_{rc}}{\gamma_r}) \qquad (9)$$

where γ_c and γ_r are the cluster and ray power decay constants, respectively.

We find that in most of the NLOS measurements, i.e., Group 2, $|\alpha_{rc}(0,0)|^2$ is not the power of the strongest MPC, and before the strongest MPC, the APDPs power increase exponentially with delay in terms of "reverse cluster". Therefore, we modify (9) by

$$|\alpha_{rc}(T_c, \tau_{rc})|^2 = \zeta \cdot |\alpha_{rc}|^2 \exp(-\frac{T'_c}{\gamma'_c}) \exp(-\frac{\tau'_{rc}}{\gamma'_r})$$
$$+ |\alpha_{rc,\max}|^2 \exp(-\frac{T''_c}{\gamma''_c}) \exp(-\frac{\tau''_{rc}}{\gamma''_r}) \qquad (10)$$

where γ_c and γ_r are the cluster and ray power decay constants. T_c and τ_{rc} represent the arrival time of the clusters and rays. We use $[\cdot]'$ and $[\cdot]''$ to represent the parameters of (10) *before* and *after* the strongest MPC, respectively. Thus, we have $\gamma'_c < 0$, $\gamma'_r < 0$, $\gamma''_c > 0$, $\gamma''_r > 0$, and

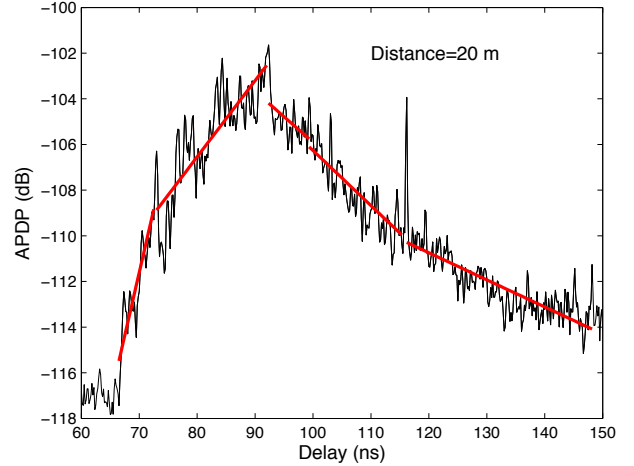$$\zeta = \begin{cases} 0, & \text{Group 1} \\ 1, & \text{Group 2} \end{cases} \qquad (11)$$

Fig. 7. Example plot of APDPs in Group 2 (NLOS, d=20 m). The red curve is the modified SV model.

$|\alpha_{rc,\max}|^2$ represents the maximum peak [4]. In the following, we use the modified model, i.e., Eq. (10), to fit the measured data. Results of these extracted parameters are available in Table. VI.

Fig. 7 shows an example plot of the measured APDPs in Group 2, together with the modified SV model [5]. The modified SV model gives good fit for the "soft onset" before the maximum peak. It is also found that there are several clearly identifiable clusters after the maximum peak in the measurements of Group 2, which is different from the observation in an industrial environment with large number of metallic scatterers [7].

V. MODEL VALIDATION

We validate the proposed model by comparing the distributions of the root-mean-square (RMS) delay spread derived from our model to that obtained from the measurement data. The RMS delay spread is defined as the second central moment of the APDP [7]

$$\tau_{\mathrm{rms}} = \sqrt{\frac{\int \hat{P}(d, S_d, \tau)\tau^2 d\tau}{\int \hat{P}(d, S_d, \tau)d\tau} - \left(\frac{\int \hat{P}(d, S_d, \tau)\tau d\tau}{\int \hat{P}(d, S_d, \tau)d\tau}\right)^2}.$$
$$(12)$$

Based on the results provided in Table VI, we synthesized the APDP. An outline of the necessary steps are provided below:

- Generate a sequence of ΔT_c from the cluster arrival rate.[6] For Group 1 and the clusters after the strongest MPC of Group 2, we arrange ΔT_c in ascending order; for the clusters before the strongest MPC of Group 2, we arrange ΔT_c in descending order. The cluster arrival time is thus expressed by

$$T_c(i+1) = T_c(i) + \Delta T_c(i). \qquad (13)$$

We normalize the first delay bin to $T_c(1) = 0$ ns.

---

[4]For Group 1, $|\alpha_{rc,\max}|^2 = |\alpha_{rc}(0,0)|^2$

[5]Measurements for Group 1 were verified, though relevant plots are not shown here due to space limitations

[6]$\frac{1}{\Lambda} = \Delta T_c \ Exp(\lambda)$

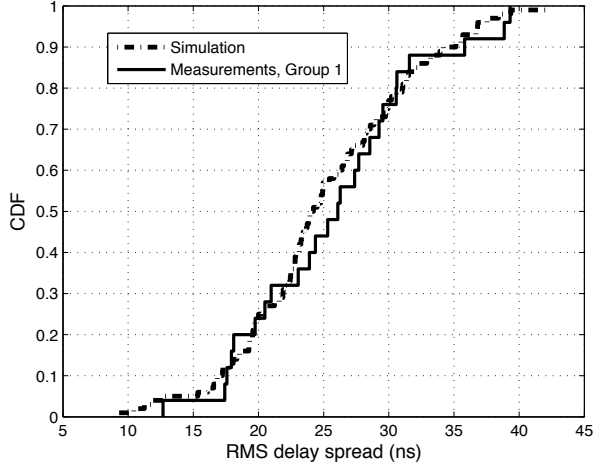|	ζ	λ'	λ''	γ'_c	γ''_c	a'	b'	a''	b''	γ'_r	γ''_r
Group 1	0	-	0.042	-	22.45	-	-	0.14	7.53	-	20.89
Group 2	1	0.055	0.039	-10.51	32.94	-0.058	-4.99	0.72	-38.94	-11.42	66.62

Fig. 8. CDFs of measured and modeled RMS delay spread for Group 1.

- Generate the power of each cluster. For Group 1, the power of the first delay bin is normalized to 0 dB, and the power of the following clusters are obtained by using the Cluster power decay ; For Group 2, we first generate the clusters using γ'_c, then we normalize the power of the last delay bin to 0 dB, and we finally use γ''_c to generate the clusters after the peak.
- Generate the power of each ray in an equivalent manner. The ray power decay constant (γ_r) in each cluster can be obtained by $\gamma_r = a \cdot \tau[ns] + b + X_{\gamma_r}$, where X_{γ_r} is a $N(0, \sigma_r)$. The interval of the delay bins is 0.17 ns, which is same to the measurements.

Fig. 8 show a comparison of the τ_{rms} statistics between the model and the measurements. It is clearly observable that the model is in good agreement with measurements. We stress, however, that this only shows that the model is suitable for fitting the data based on which it was derived. Complementary measurements in other warehouses would be required to validate how much the parameters change from warehouse to warehouse. This is, however, a challenge often encountered in channel modeling - as a matter of fact most UWB channel models are based on a single measurement campaign in a specific location only.

VI. SUMMARY AND CONCLUSION

We conducted a measurement campaign in a warehouse environment using frequency domain channel sounder setup. We extracted parameters required for modeling the propagation channel characteristics. We find that distance-dependent pathloss exponent (n) to be 1.63 in LOS scenario and 2.14 in the NLOS scenario, we also find the frequency-dependent pathloss (κ) to be 1.3 for both LOS and NLOS scenarios, while the standard deviation of the shadowing ($N(0, \sigma_{dB})$) is

2.86 and 2.84dB for the LOS and NLOS respectively. We performed a clustering analysis and found that the APDP in the LOS and NLOS scenarios can be divided into two different groups based on delay index of strongest MPCs in the environment. All extracted classical cluster parameters are listed in Table VI. The small - scale fading statistics were modeled using a Nakagami m distribution. The m-parameters themselves are random variables and as such as modeled as truncated Gaussian distribution; mean and variance decreased with delay.

REFERENCES

[1] M. Di Benedetto and G. Giancola, *Understanding Ultra Wide Band Radio Fundamentals*, ser. Prentice Hall communications engineering and emerging technologies series. Pearson Education, 2004.
[2] "First report and order 02-48," Federal Communications Commission, Tech. Rep., 2002.
[3] M. Win and R. Scholtz, "Impulse radio: how it works," *Communications Letters, IEEE*, vol. 2, no. 2, pp. 36–38, 1998.
[4] S. Gezici, Z. Tian, G. Giannakis, H. Kobayashi, A. Molisch, H. Poor, and Z. Sahinoglu, "Localization via ultra-wideband radios: a look at positioning aspects for future sensor networks," *Signal Processing Magazine, IEEE*, vol. 22, no. 4, pp. 70–84, 2005.
[5] S. Savazzi and U. Spagnolin, "Synchronous ultra-wide band wireless sensors networks for oil and gas exploration," in *Computers and Communications, 2009. ISCC 2009. IEEE Symposium on*, July 2009, pp. 907–912.
[6] C.-C. Chong and S. K. Yong, "A generic statistical-based uwb channel model for high-rise apartments," *Antennas and Propagation, IEEE Transactions on*, vol. 53, no. 8, pp. 2389–2399, 2005.
[7] J. Karedal, S. Wyne, P. Almers, F. Tufvesson, and A. F. Molisch, "A measurement-based statistical model for industrial ultra-wideband channels," *Wireless Communications, IEEE Transactions on*, vol. 6, no. 8, pp. 3028–3037, 2007.
[8] S. Sangodoyin, V. Kristem, A. F. Molisch, H. Ruisi, and F. Tufvesson, "Statistical modeling of ultrawideband mimo propagation channel in a warehouse environment," *Wireless Communications, IEEE Transactions on*, to be submitted.
[9] A. F. Molisch, "Ultrawideband propagation channels-theory, measurement, and modeling," *IEEE Transactions on Vehicular Technology*, vol. 54, pp. 1528–1545, Sep. 2005.
[10] J. Kunisch and J. Pamp, "Measurement results and modeling aspects for the uwb radio channel," in *Ultra Wideband Systems and Technologies, 2002. Digest of Papers. 2002 IEEE Conference on*, May 2002, pp. 19–23.
[11] D. Cassioli, M. Win, and A. Molisch, "The ultra-wideband bandwidth indoor channel:from statistical models to simulations," *IEEE J. Sel. Areas Commun.*, vol. 20, pp. 1247–1257, Aug 2002.
[12] A. A. Saleh and R. Valenzuela, "A statistical model for indoor multipath propagation," *Selected Areas in Communications, IEEE Journal on*, vol. 5, no. 2, pp. 128–137, 1987.